ADVANCED OPTICAL MATERIALS
www.advopticalmat.de



# Optical Multiparameter Detection System Based on a Broadband Achromatic Metalens Array

*Xing Feng, Yuxi Wang, Yunxuan Wei, Tie Hu, Shunyuan Xiao, Guangqiang He, Ming Zhao,* Jinsong Xia,* and Zhenyu Yang**

**Metalenses, known as flat metasurface lenses based on subwavelength phase modulations, have been widely applied to compact and multifunctional optical devices due to their high flexibility in controlling light. However, most metalenses only operate at single wavelength, limiting their practical applications. In this paper, an achromatic metalens array (AMLA)-based optical multiparameter detection system, for a near-infrared spectrum from 1310 to 1550 nm, is reported. Such system can simultaneously detect the spatially varying polarization and phase gradient of the broadband beam. Its performance is experimentally characterized at wavelengths of 1310, 1430, and 1550 nm. Average errors of 18 selected polarization states are respectively 6.40%, 6.74%, and 6.02%. Average errors of phase gradients of seven different incident light are 8.93%, 7.44%, and 5.68%. This system can find applications in structured light detection, quantum optics, and polarization imaging.**

## 1. Introduction

Metasurfaces, famous for the flexibility in manipulating the phase and polarization of light, have been widely used in beam shaping,[1–5] polarization modulations,[6–11] holograms,[12–16] optical stealth,[17–19] and especially planar metalenses.[20–28] Owing to high compactness and no spherical aberrations, metalenses have broad application prospects in optical focusing, imaging and detections. In previous works,[29,30] we have demonstrated a dielectric metalens array for multiparameter detection, operating at the wavelength of 1550 nm. Compared with traditional methods, our system can simultaneously measure the polarization and wavefront of the incident light. However, the large dispersion of the metalens limits the detection system to single wavelength.

Up to now, achromatic metalenses have aroused great interests[31–35] and been realized through mainly three methods. First, meta-atoms[36] and spatial multiplexing methods[37,38] are raised for multiwavelength metalenses. Second, cascaded metasurfaces are used to guide light along the predetermined trajectory to achieve achromatic focusing.[39,40] Finally, various works based on dispersion manipulation principles have been proposed in recent years, including Wang et al.'s phase shift method and Capasso and co-workers delay method.[41–44] In summary, achromatic metalenses are becoming mature and practical.

Here, we propose and experimentally demonstrate an achromatic metalens array (AMLA) based broadband optical multiparameter detection system. The polarization and wavefront of the incident beam can be simultaneously acquired from the intensity and the shift of the focal point. The achromatic focusing ability of the AMLA is verified at the wavelength of 1310, 1430, and 1550 nm. We also test its detection performances with 18 different polarization states and eight different incident angles at three wavelengths. All results show that this multiparameter detection system can work for broadband optical measurements. This system will provide a platform for measuring various parameters of the beam. Based on this design, the working wavelength of the metalens array can be extended to any desired spectrum, which has great potential in other fields such as polarization imaging, biomedical diagnosis, optical communication, atmospheric interference measurement, and quantum communication.

Dr. X. Feng, Dr. Y. X. Wang, Y. X. Wei, Dr. T. Hu, S. Y. Xiao, Prof. M. Zhao, Prof. J. S. Xia, Prof. Z. Y. Yang
Wuhan National Laboratory for Optoelectronics
School of Optical and Electronic Information
Huazhong University of Science and Technology (HUST)
Wuhan 430074, China
E-mail: zhaoming@hust.edu.cn; jsxia@hust.edu.cn; zyang@hust.edu.cn
Prof. G. Q. He
State Key Laboratory of Advanced Optical Communication Systems and Networks
Department of Electronic Engineering
Shanghai Jiao Tong University
Shanghai 200240, China
The ORCID identification number(s) for the author(s) of this article can be found under https://doi.org/10.1002/adom.202100772.

DOI: 10.1002/adom.202100772

## 2. Designs and Principles

Detection principles of the broadband optical multi-parameter detection system are shown in **Figure 1**a. Each pixel of the AMLA contains four polarization-dependent achromatic metalenses which only focus certain polarization components of light. The focal points shift when the incident phase gradient changes. Therefore, the polarization state and the phase gradient of the incident light can be both restored at the same time, from the intensity and the position of the focal point. The

 

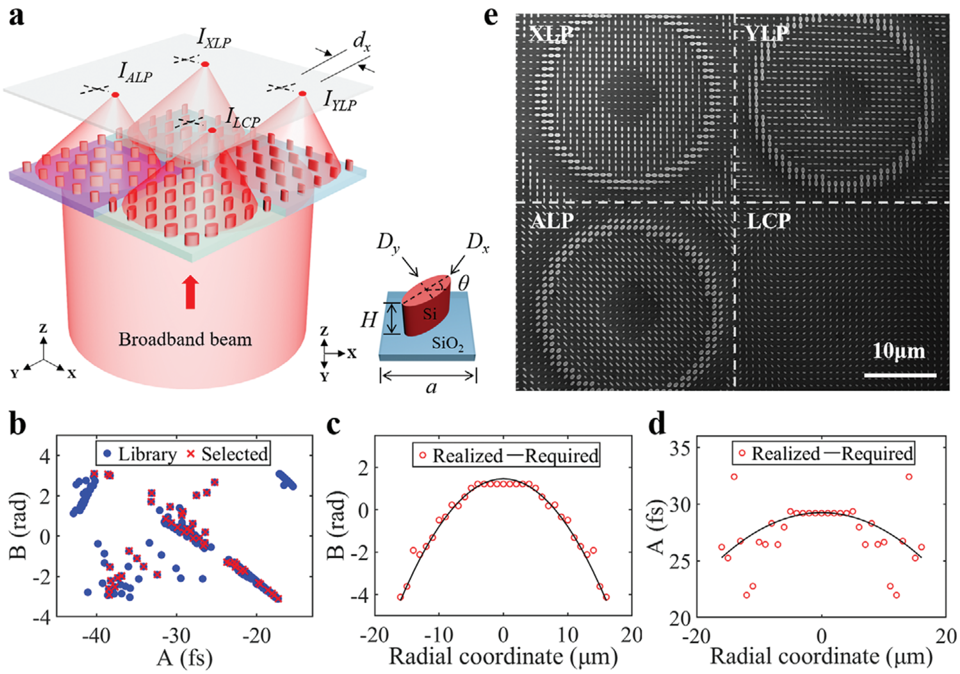


**Figure 1.** Design of the achromatic metalens array. a) Scheme of the AMLA pixel consisting of four polarization-sensitive achromatic metalenses and the unit element. Incident polarizations and phase gradients are reconstructed from the intensities and shifts of the focal points. b) Fitting results of all unit elements in the library (blue points) and the values (red cross) of the selected unit elements of the XLP achromatic metalens. $A$ is the slope and $B$ is the intercept, for the fitting function $\phi(\omega) = A\omega + B$. c,d) Realized (red circles) and required (black curves) $B$ and $A$ at each radial coordinate of the XLP achromatic metalens. e) Scanning electron micrograph of one pixel in the AMLA. The scale bar is 10 µm.

achromatic metalenses are composed of silicon elliptical pillars with a period of 900 nm and a height of 1400 nm, upon a quartz substrate (Figure 1a). The phase and transmittance of the elliptical pillar are adjusted by varying its major axis $D_x$, minor axis $D_y$ and orientation angle $\theta$. The general phase profile of a metalens is[20]

$$\varphi(r,\omega) = -\frac{\omega}{c}\left(\sqrt{r^2+F^2}-F\right)+C \tag{1}$$

where $r$ is the radial coordinate, $\omega$ is the incident frequency, $F$ is the focal length, and $C$ is a constant bias. The diffraction, and the nanopillar's frequency sensitive electromagnetic response coming from the material dispersion and the resonant mode dispersion, both contribute to the chromatism of the metalens. By carefully selecting pillars whose frequency sensitive phases match Equation (1) well, the diffractive dispersion can be compensated and thus the achromatic metalens is achieved.

In our AMLA, every metalens is set to operate for the infrared band from 1310 to 1550 nm, with a width of 29.7 µm and a numerical aperture (NA) of 0.21. For linearly polarized metalenses, we numerically calculate the propagation phase of each unit element under the $x$ linear polarized (XLP) incidence with a broadband spectrum from 1310 to 1550 nm, through the finite-difference time-domain (FDTD) approach. We then fit the curve of the phase versus the frequency with the linear function $\phi(\omega) = A\omega + B$. Unit elements with fitting errors less than 1% are chosen to construct the library. The fitting error is defined as the average relative absolute error between the fitting curve and the simulation phase. Figure 1b–d separately exhibit the library, the phase contributions on the radial direction, the fitting slops on the radial direction, for the XLP achromatic metalens at the wavelength of 1430 nm. The y linearly polarized (YLP) and the 45° linearly polarized (ALP) metalenses are realized by rotating the same pillars of the XLP metalens by 90° and 45°, respectively. The left circularly polarized (LCP) metalens, whose simulation results are listed in Section S1, Supporting Information, is designed with the similar method. However, because with an extreme height of 1400 nm, the selected pillars in LCP metalens are hard to be processed with simultaneously accurate $D_x$, $D_y$, and $\theta$. Meantime, part of the $D_x$ and $D_y$ are smaller than the minimum feature size. Both of them result the poor focusing performance of the achromatic LCP metalens. Therefore, we replace the achromatic LCP metalens with a dispersive LCP metalens whose NA is also 0.21 at the wavelength of 1430 nm. Because of the usage of the PB phase,[45,46] all nanopillars in the dispersive LCP metalens are with the same long and short axis of $D_x =$ 260 nm and $D_y =$ 340 nm, which are easier to be fabricated.

As revealed in Figure 1a, a group of XLP, YLP, ALP, and LCP metalenses, separately focusing four polarization components of the incidence into four different focal points, composes an AMLA pixel. The focusing intensities $I_{\mathrm{XLP}}$, $I_{\mathrm{YLP}}$, $I_{\mathrm{ALP}}$, and $I_{\mathrm{LCP}}$ characterize the Stokes parameters by the equation set[47–49]

$$\begin{cases} S_0 = I_x + I_y = I_{\mathrm{XLP}} + I_{\mathrm{YLP}} \\ S_1 = I_x - I_y = I_{\mathrm{XLP}} - I_{\mathrm{YLP}} \\ S_2 = I_a - I_b = 2I_{\mathrm{ALP}} - I_{\mathrm{XLP}} - I_{\mathrm{YLP}} \\ S_3 = I_l - I_r = 2I_{\mathrm{LCP}} - I_{\mathrm{XLP}} - I_{\mathrm{YLP}} \end{cases} \tag{2}$$

where $I_x$, $I_y$, $I_a$, $I_b$, $I_r$, and $I_l$ refer to the intensity of the $x$ linear, $y$ linear, 45° linear, −45° linear, right-circular and left-circular polarization components of the incident light. Moreover, following the concept of the Hartmann–Shark wavefront sensor,[50,51] phase gradients of the incident light can be acquired from the positions of every focal points, through the relationship

$$\frac{\partial\Phi}{\partial x} = \frac{2\pi}{\lambda}\cdot\frac{d_x}{\sqrt{f^2+d_x^2}} \tag{3}$$

$$\alpha = \arcsin\left(\frac{d_x}{\sqrt{f^2+d_x^2}}\right) \tag{4}$$

where $\partial\Phi/\partial x$ indicates the phase gradient of the incident light along the $x$ axis. $d_x$ is the focal position offset and $\alpha$ is the incident angle. An AMLA usually contains multiple pixels, thus able to detect space variant polarization states and phase gradients.

To verify the performance of our design, we fabricated an AMLA composed of an array of 10 × 10 pixels. Figure 1e shows the scanning electron micrograph of the fabricated sample (the fabrication process and scanning electron image of the AMLA are in Section S2 in the Supporting Information).

## 3. Results and Discussions

### 3.1. Characterization of the Achromatic Metalenses

The focusing performances of the XLP and LCP metalenses are shown in **Figure 2**. Figure 2a,b, respectively for the XLP and the LCP metalens, depict the experimental field intensity in the $x$–$z$ plane and the focal plane at three wavelengths. Although the focal length slightly changes at different wavelengths, both XLP and LCP incident light can be focused in the detection plane because of the long focal depth. Measured and simulated focal lengths are collected in **Figure 3**a (detailed simulation results are in Section S3 in the Supporting Information). Simulated focal lengths of the XLP and LCP metalenses both change slightly around the target 70 µm. The measured focal length of the XLP metalens varies a little but deviates obviously from the simulation result. Here, the deviation is partly attributed to manufacture errors. To eliminate

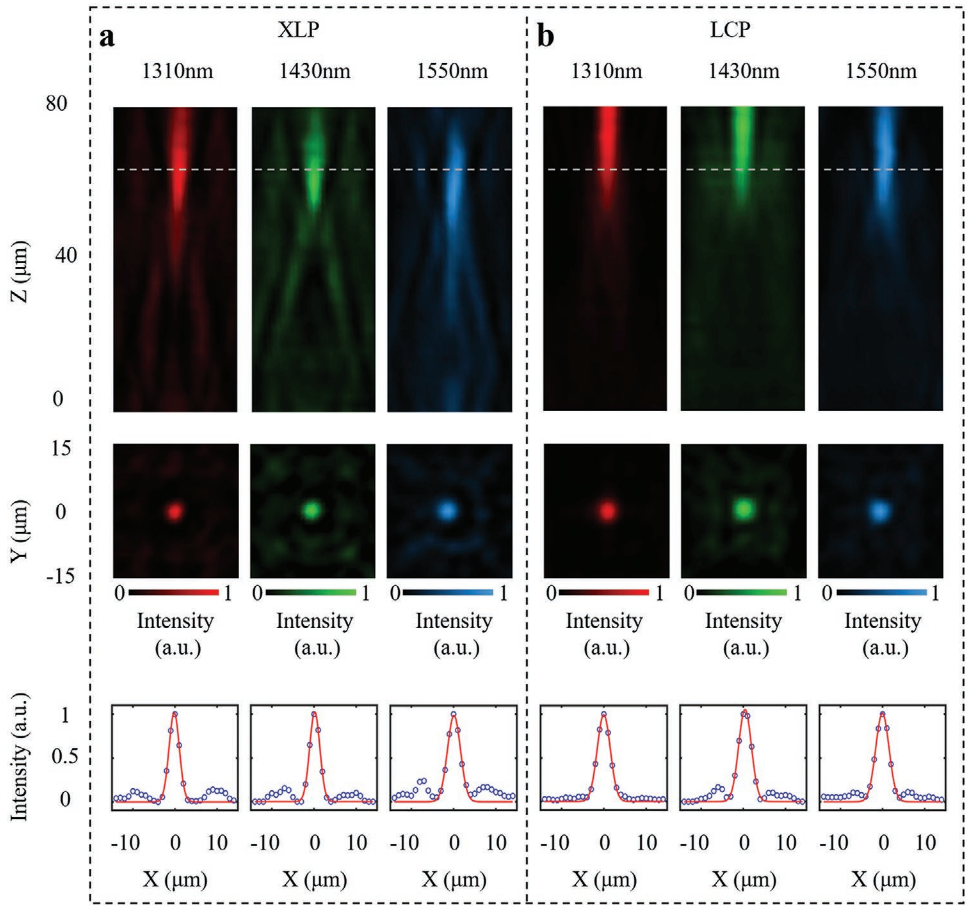


**Figure 2.** Focusing performances of the XLP and LCP metalenses. a,b) Normalized measured intensity distributions at the wavelength of 1310, 1430, and 1550 nm, for a) the XLP metalens and b) the LCP metalens. Focal planes are marked with white dashed lines, and shown in the bottom. Red solid lines depict Gaussian fitting results.

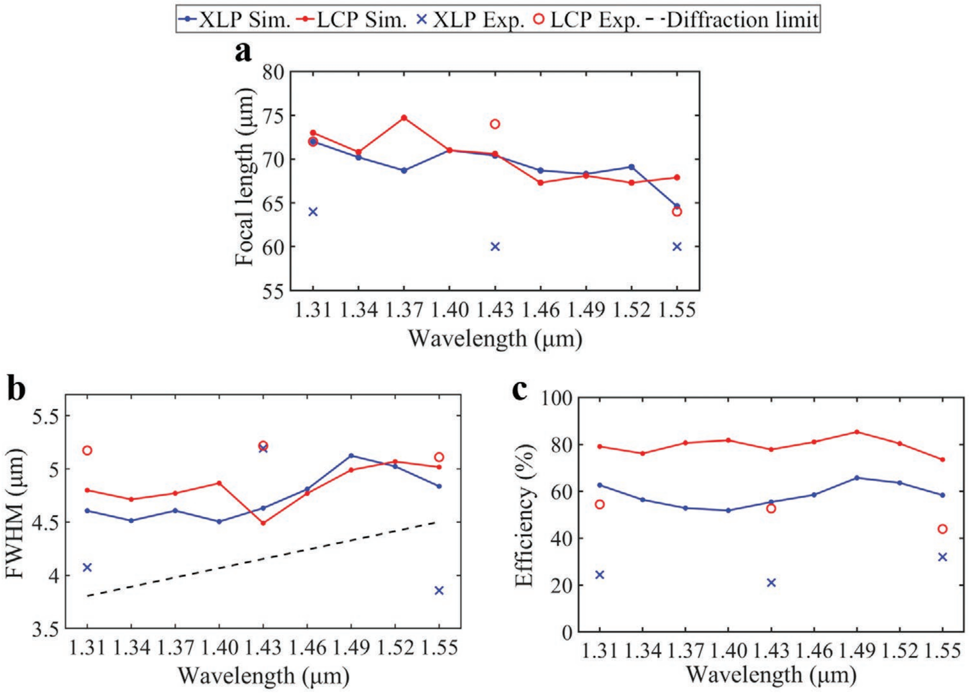


**Figure 3.** Results of simulations and experiments. a) Focal lengths, b) FWHM, c) efficiencies. All experimental results are plotted with isolated crosses and circles, and simulated ones are with lines. The dashed line in (b) indicates the diffraction limit.

such errors, scanning electron microscopy can be applied during the fabrication to improve size accuracy. Meantime, unit elements with higher manufacturing error tolerance can be selected on the bias of the fabrication condition. In addition, by increasing geometric freedom of unit elements, those elements with higher transmittances and more precise dispersion slops might be found to optimize the performance of the metalens. The full width at half maxima (FWHM) and the focusing efficiencies are shown in Figure 3b,c. The FWHM is calculated by 2.335 times of the standard deviation of the fitting Gaussian function. The efficiency is defined as the ratio of the power in a circular area with a diameter of three times of the FWHM to the total power in the focal plane. According to the simulation, both XLP and LCP metalenses can focus the incidence into the near diffraction limit (0.514 $\lambda/NA$), with average efficiencies of 58.31% and 79.45% respectively. The experimental FWHM is still close to the diffraction limit whereas the average efficiencies of the XLP and LCP metalenses decrease to 25.75% and 50.29%, which also mainly comes from the fabrication error.

different polarization states and at three wavelengths. Totally 18 Stokes parameters $S_1$, $S_2$, and $S_3$ are then measured with this pixel. Corresponding detection results are characterized with the Poincare sphere in Figure 4c. The errors of the 18 polarization states detected at 1310, 1430, and 1550 nm are 6.40%, 6.74%, and 6.02%, respectively. The relative mean square of each polarization is calculated as $\sqrt{(S_1^{'}-S_1)^2+(S_2^{'}-S_2)^2+(S_3^{'}-S_3)^2}/S_0$, where $S_1^{'}$, $S_2^{'}$, and $S_3^{'}$ are the measured Stokes paraments, $S_0$, $S_1$, $S_2$, and $S_3$ are the theoretical values. The error of polarization is defined as the average of the relative mean squares of 18 polarization states. Experimentally reconstructed Stokes parameters and their theoretical values are recorded in Table S1 in the Supporting Information. Average detection errors of elliptical polarizations are 175% larger than those of linear polarizations, which contribute primarily to the total error. We attribute this to the mismatch between the focal lengths of the linearly polarized metalenses and the LCP metalens, as the focal plane of the former is chosen as the observation plane. (See Table S2 in the Supporting Information for the simulation results of polarization state detection at other wavelengths).

### 3.2. Polarization Detection

Optical setup for the polarization detection is exhibited in **Figure 4**a. The half or quarter wave plate and the polarizer are used to generate an arbitrary polarized incident beam. Here, the horizontal, vertical and 45° linear polarizations, and the left-circular polarization are detected with the AMLA first to construct a reconstruction matrix for accurately reconstructing Stokes parameters.[47–49] Figure 4b shows focal plane intensity distributions of an AMLA pixel, under the normal incidences with

### 3.3. Wavefront Detection

The experimental setup in **Figure 5**a is used to demonstrate the wavefront detection capacity of the AMLA. The collimated XLP illumination, at different wavelengths of 1310, 1430, and 1550 nm, is deflected in the $x$–$z$ plane, with different intersection angles of 0.5°, 1°, 2°, 5°, 8°, 10°, 12° to z axis. Figure 5b shows focal plane intensities of one AMLA pixel under different incident angles, at the wavelength of 1310 nm (see Section S4, Supporting Information for results at 1430 and 1550 nm). As

 

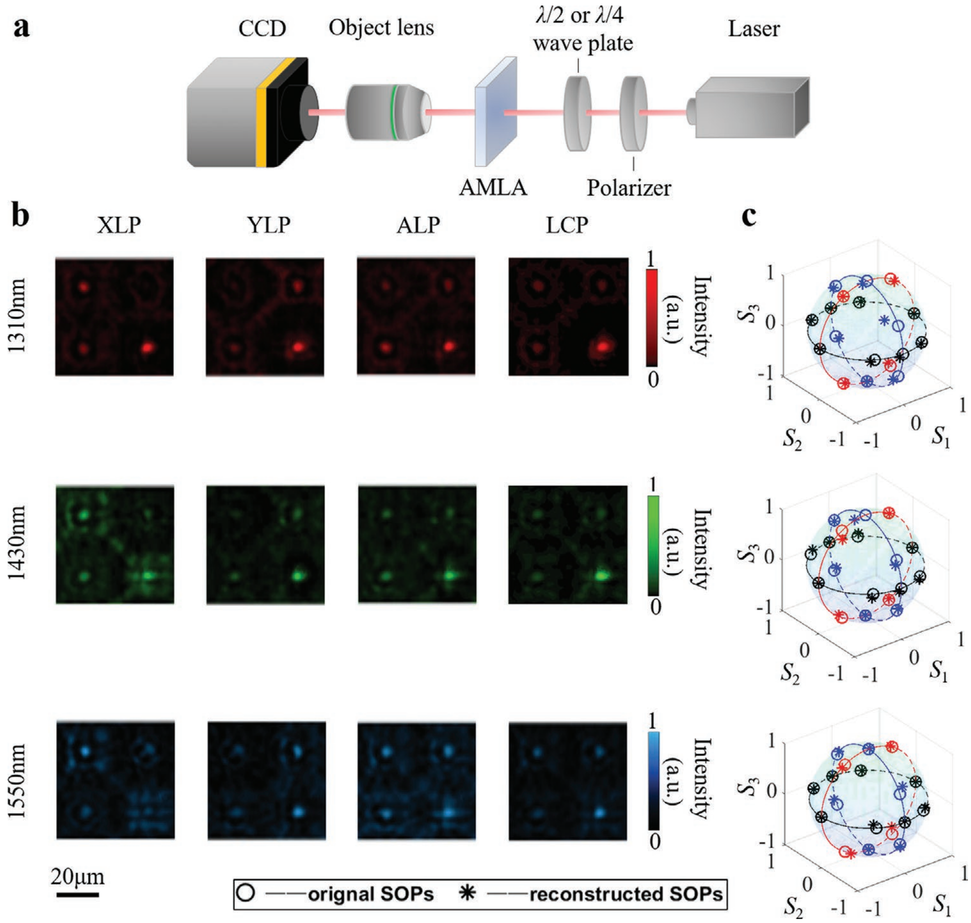


**Figure 4.** Experimental setup and results of the polarization detection with the AMLA. a) Optical setup for polarization detection. Incident polarizations are generated with the XLP polarizer and the wave plate. A 20× object lens is put in front of the CCD to observe the focal field. b) Normalized intensity distributions in the focal plane of one selected pixel, under the XLP, YLP, ALP, and LCP light at wavelengths of 1310, 1430, 1550 nm. The scale bar is 20 µm. c) Detected Stokes parameters (stars) and theoretical predictions (circles) on a Poincare sphere. Red, black, and blue lines denote the positions where $S_1$, $S_2$, and $S_3$ are respectively 0.

to be expected, focal spots shift greater from the center under larger incident angles. The centroid of the focal spot is calculated to identify the focusing position, so the phase gradient of the incident light can be reconstructed even when the focal spot shifts less than one charge coupled device (CCD) pixel, for example, under the incident angle of 0.5°. When the incident angle reaches 12°, the focal spot almost reaches the bound of the corresponding metalens, representing the largest detectable phase gradient. The maximum detectable phase gradient can be improved by a sorting method algorithm.[52] Figure 5c summarizes the wavefront detection results at three wavelengths. For 1310, 1430, and 1550 nm, the errors of the phase gradients are 8.93%, 7.44%, and 5.68%. The measured phase gradient $G$ is calculated by Equation S6 in the Supporting Information. The theoretical value $G_0$ is defined as $\sin(\theta) \cdot 2\pi/\lambda$, where $\theta$ is the incident angle. The relative error of the phase gradient is calculated by $(G - G_0)/G_0$. The error of the phase gradient at one wavelength is defined as the average of the relative errors at seven different angles. The limit spatial resolution of the CCD contributes to errors. Our AMLA has a longer focal length of 70 µm compared with the previous work[29] of 30 µm, so it is more sensitive to tiny phase gradients. In order to maintain the NA, we increase the diameter of the metalens, in the cost of the detectably spatial resolution. (See Table S3 in the Supporting Information for the simulation results of wavefront detection at other wavelengths).

## 4. Conclusion

In summary, we have demonstrated a broadband polarization and wavefront detection system based on the AMLA, through both simulations and experiments. In our system, polarization-sensitive metalenses decompose the incidence into different polarization states, while their achromatic properties ensure to focus the light, within an infrared band from 1310 to 1550 nm, to nearly the same position. The spatial polarization state and the phase gradient of the incident light are simultaneously acquired from the focusing behavior. The semiconductor-compatible processing technology promises to integrate the AMLA with the CCD to form a compact multiparameter detection camera for communication bands. By changing materials and designing unit elements with higher degrees of freedom, this design can also be applied to other bands.

 

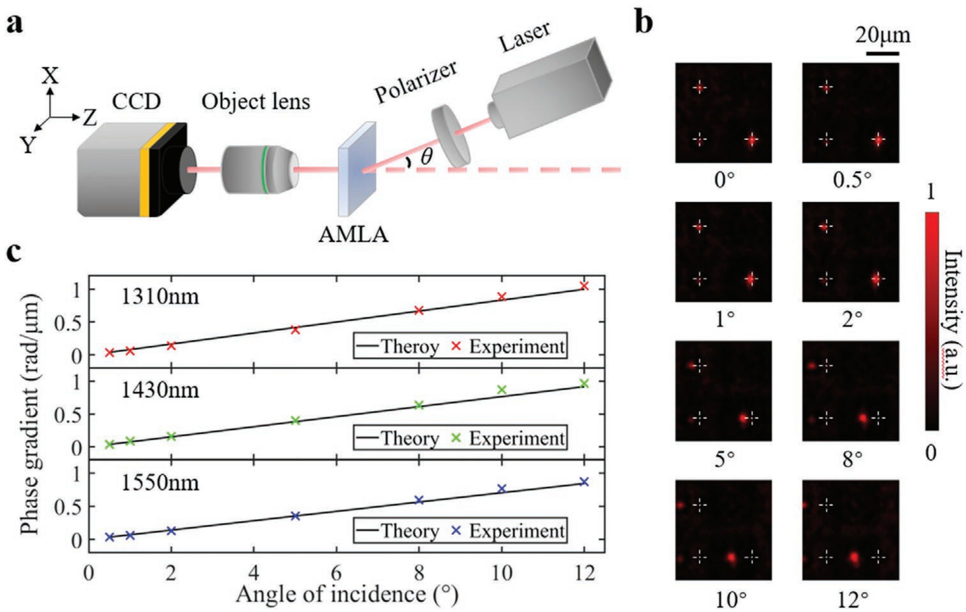


**Figure 5.** Experimental setup and results of the wavefront detection with the AMLA. a) Optical setup for wavefront detection. b) Normalized intensity distributions in the focal plane of one selected pixel, under the illumination with eight incident angles at the wavelength of 1310 nm. Dashed crosses mark the central position of each metalens. The scale bar is 10 µm. c) Experimentally measured phase gradients (crosses) at different incident angles and wavelengths. Black solid lines represent theoretical values.

## Supporting Information

Supporting Information is available from the Wiley Online Library or from the author.

## Acknowledgements

This work was supported by the Natural Science Foundation of China under Grant 61835008, 62075073, 61905079, 61905084, the Fundamental Research Funds for the Central Universities, No. 2019kfyXKJC038, the State Key Laboratory of Advanced Optical Communication Systems and Networks of Shanghai Jiao Tong University, China (2021GZKF007), and the Natural Science Foundation of Hubei Province, No. 2019CFB438.

## Conflict of Interest

The authors declare no conflict of interest.

## Author Contributions

X.F. and Y.X.W.(1) contributed equally to this work. X.F. had the idea, conceived the study, finished the simulations; Y.X.W.(1) fabricated the samples and analyzed them; X.F. performed the measurements with the help from T.H. and S.Y.X.; J.S.X. supervised the fabrication; Y.X.W.(2), G.Q.H., M.Z., and Z.Y.Y. supervised the work and the manuscript writing. All authors discussed the results. X.F. wrote a first draft of the manuscript, which was refined by contributions from all authors.

## Data Availability Statement

The data that supports the findings of this study are available in the supplementary material of this article.

## Keywords

achromatic metalens array, flat lenses, phase gradients, polarization

Received: April 15, 2021
Revised: May 28, 2021
Published online: July 1, 2021

[1] J. Scheuer, *Nanophotonics* **2017**, *6*, 137.
[2] S. Keren-Zur, O. Avayu, L. Michaeli, T. Ellenbogen, *ACS Photonics* **2015**, *3*, 117.
[3] O. Avayu, O. Eisenbach, R. Ditcovski, T. Ellenbogen, *Opt. Lett.* **2014**, *39*, 3892.
[4] B. Desiatov, N. Mazurski, Y. Fainman, U. Levy, *Opt. Express* **2015**, *23*, 22611.
[5] A. L. Holsteen, A. F. Cihan, M. L. Brongersma, *Science* **2019**, *365*, 257.
[6] N. Yu, F. Aieta, P. Genevet, M. A. Kats, Z. Gaburro, F. Capasso, *Nano Lett.* **2012**, *12*, 6328.
[7] Y. Yang, W. Wang, P. Moitra, KravchenkoII, D. P. Briggs, J. Valentine, *Nano Lett.* **2014**, *14*, 1394.
[8] C. Pfeiffer, C. Zhang, V. Ray, L. J. Guo, A. Grbic, *Phys. Rev. Lett.* **2014**, *113*, 023902.
[9] Q. Levesque, M. Makhsiyan, P. Bouchon, F. Pardo, J. Jaeck, N. Bardou, C. Dupuis, R. Haidar, J. L. Pelouard, *Appl. Phys. Lett.* **2014**, *104*, 111105.
[10] N. K. Grady, J. E. Heyes, D. R. Chowdhury, Y. Zeng, M. T. Reiten, A. K. Azad, A. J. Taylor, D. A. R. Dalvit, H. T. Chen, *Science* **2013**, *340*, 1304.
[11] G.-X. Dong, H.-Y. Shi, S. Xia, W. Li, A.-X. Zhang, Z. Xu, X.-Y. Wei, *Chin. Phys. B* **2016**, *25*, 084202.
[12] Y. W. Huang, W. T. Chen, W. Y. Tsai, P. C. Wu, C. M. Wang, G. Sun, D. P. Tsai, *Nano Lett.* **2015**, *15*, 3122.
[13] S. Larouche, Y. J. Tsai, T. Tyler, N. M. Jokerst, D. R. Smith, *Nat. Mater.* **2012**, *11*, 450.
[14] X. Ni, A. V. Kildishev, V. M. Shalaev, *Nat. Commun.* **2013**, *4*, 2807.
[15] G. Zheng, H. Muhlenbernd, M. Kenney, G. Li, T. Zentgraf, S. Zhang, *Nat. Nanotechnol.* **2015**, *10*, 308.

[16] X. Song, L. L. Huang, C. C. Tang, J. J. Li, X. W. Li, J. Liu, Y. T. Wang, T. Zentgraf, *Adv. Opt. Mater.* **2018**, *6*, 1701181.
[17] Y. Yang, L. Jing, B. Zheng, R. Hao, W. Yin, E. Li, C. M. Soukoulis, H. Chen, *Adv. Mater.* **2016**, *28*, 6866.
[18] J. Zhang, Z. Lei Mei, W. Ru Zhang, F. Yang, T. Jun Cui, *Appl. Phys. Lett.* **2013**, *103*, 151115.
[19] X. Ni, Z. J. Wong, M. Mrejen, Y. Wang, X. Zhang, *Science* **2015**, *349*, 1310.
[20] F. Aieta, P. Genevet, M. A. Kats, N. Yu, R. Blanchard, Z. Gaburro, F. Capasso, *Nano Lett.* **2012**, *12*, 4932.
[21] Y. Wei, Y. Wang, X. Feng, S. Xiao, Z. Wang, T. Hu, M. Hu, J. Song, M. Wegener, M. Zhao, J. Xia, Z. Yang, *Adv. Opt. Mater.* **2020**, *8*, 2000142.
[22] X. Chen, L. Huang, H. Muhlenbernd, G. Li, B. Bai, Q. Tan, G. Jin, C. W. Qiu, S. Zhang, T. Zentgraf, *Nat. Commun.* **2012**, *3*, 1198.
[23] D. Lu, Z. Liu, *Nat. Commun.* **2012**, *3*, 1205.
[24] P. Lalanne, P. Chavel, *Laser Photon. Rev.* **2017**, *11*, 1600295.
[25] M. L. Tseng, H.-H. Hsiao, C. H. Chu, M. K. Chen, G. Sun, A.-Q. Liu, D. P. Tsai, *Adv. Opt. Mater.* **2018**, *6*, 1800554.
[26] M. Khorasaninejad, W. T. Chen, A. Y. Zhu, J. Oh, R. C. Devlin, D. Rousso, F. Capasso, *Nano Lett.* **2016**, *16*, 4595.
[27] L. Verslegers, P. B. Catrysse, Z. F. Yu, J. S. White, E. S. Barnard, M. L. Brongersma, S. H. Fan, *Nano Lett.* **2009**, *9*, 235.
[28] H. Liang, Q. Lin, X. Xie, Q. Sun, Y. Wang, L. Zhou, L. Liu, X. Yu, J. Zhou, T. F. Krauss, J. Li, *Nano Lett.* **2018**, *18*, 4460.
[29] Y. Wang, Z. Wang, X. Feng, M. Zhao, C. Zeng, G. He, Z. Yang, Y. Zheng, J. Xia, *Photonics Res.* **2020**, *8*, 482.
[30] Z. Yang, Z. Wang, Y. Wang, X. Feng, M. Zhao, Z. Wan, L. Zhu, J. Liu, Y. Huang, J. Xia, M. Wegener, *Nat. Commun.* **2018**, *9*, 4607.
[31] B. Xiong, J. N. Wang, R. W. Peng, H. Jing, R. H. Fan, D. X. Qi, F. Chen, M. Wang, *Adv. Opt. Mater.* **2020**, *9*, 2001524.
[32] W. T. Chen, A. Y. Zhu, F. Capasso, *Nat. Rev. Mater.* **2020**, *5*, 604.
[33] A. Ndao, L. Hsu, J. Ha, J. H. Park, C. Chang-Hasnain, B. Kante, *Nat. Commun.* **2020**, *11*, 3205.
[34] S. Colburn, A. Majumdar, *ACS Photonics* **2019**, *7*, 120.
[35] S. Shrestha, A. C. Overvig, M. Lu, A. Stein, N. Yu, *Light: Sci. Appl.* **2018**, *7*, 85.
[36] E. Arbabi, A. Arbabi, S. M. Kamali, Y. Horie, A. Faraon, *Optica* **2016**, *3*, 628.
[37] O. Avayu, E. Almeida, Y. Prior, T. Ellenbogen, *Nat. Commun.* **2017**, *8*, 14992.
[38] K. Li, Y. Guo, M. Pu, X. Li, X. Ma, Z. Zhao, X. Luo, *Opt. Express* **2017**, *25*, 21419.
[39] A. McClung, M. Mansouree, A. Arbabi, *Light: Sci. Appl.* **2020**, *9*, 93.
[40] F. Balli, M. Sultan, S. K. Lami, J. T. Hastings, *Nat. Commun.* **2020**, *11*, 3892.
[41] W. T. Chen, A. Y. Zhu, V. Sanjeev, M. Khorasaninejad, Z. Shi, E. Lee, F. Capasso, *Nat. Nanotechnol.* **2018**, *13*, 220.
[42] S. Wang, P. C. Wu, V. C. Su, Y. C. Lai, M. K. Chen, H. Y. Kuo, B. H. Chen, Y. H. Chen, T. T. Huang, J. H. Wang, R. M. Lin, C. H. Kuan, T. Li, Z. Wang, S. Zhu, D. P. Tsai, *Nat. Nanotechnol.* **2018**, *13*, 227.
[43] S. Wang, P. C. Wu, V. C. Su, Y. C. Lai, C. Hung Chu, J. W. Chen, S. H. Lu, J. Chen, B. Xu, C. H. Kuan, T. Li, S. Zhu, D. P. Tsai, *Nat. Commun.* **2017**, *8*, 187.
[44] W. T. Chen, A. Y. Zhu, J. Sisler, Z. Bharwani, F. Capasso, *Nat. Commun.* **2019**, *10*, 355.
[45] J. P. Balthasar Mueller, N. A. Rubin, R. C. Devlin, B. Groever, F. Capasso, *Phys. Rev. Lett.* **2017**, *118*, 113901.
[46] E. Hasman, V. Kleiner, G. Biener, A. Niv, *Appl. Phys. Lett.* **2003**, *82*, 328.
[47] S. Wei, Z. Yang, M. Zhao, *Opt. Lett.* **2017**, *42*, 1580.
[48] F. Gori, *Opt. Lett.* **1999**, *24*, 584.
[49] A. Pors, S. I. Bozhevolnyi, *Phys. Rev. Appl.* **2016**, *5*, 064015.
[50] B. C. Platt, R. Shack, *J. Refractive Surg.* **2001**, *17*, S573.
[51] F. A. Starikov, G. G. Kochemasov, S. M. Kulikov, A. N. Manachinsky, N. V. Maslov, A. V. Ogorodnikov, S. A. Sukharev, V. P. Aksenov, I. V. Izmailov, F. Y. Kanev, V. V. Atuchin, I. S. Soldatenkov, *Opt. Lett.* **2007**, *32*, 2291.
[52] J. W. Lee, R. V. Shack, M. R. Descour, *Appl. Opt.* **2005**, *44*, 4838.